Polarization-resolved near-backscattering of airborne aggregates composed of different primary particles

Brandon Redding,[1] Yong-Le Pan,[2] Chuji Wang,[2,3] and Hui Cao[1,*]

[1]*Department of Applied Physics, Yale University, New Haven, Connecticut 06520, USA*

[2]*U.S. Army Research Laboratory, Adelphi, Maryland 20783, USA*

[3]*Department of Physics, Mississippi State University, Starkville, Mississippi 39759, USA*

**Corresponding author: hui.cao@yale.edu*

Received May 16, 2014; revised June 6, 2014; accepted June 6, 2014;
posted June 6, 2014 (Doc. ID 212249); published July 2, 2014

We measured the polarization-resolved angular elastic scattering intensity distribution of aggregates composed of primary particles with different shapes and packing densities in the near-backward directions (155°–180°). Specifically, we compare aggregates composed of spherical polystyrene latex spheres, cylinder-like *Bacillus subtilis* particles, and Arizona road dust, as well as tryptophan particles. We observe clearly differentiable polarization aspect ratios and find that the negative polarization dip is more pronounced in more densely packed aggregates or particles. This work indicates that the polarization aspect ratio in the near-backward direction may be used as a fingerprint to discriminate between aggregates with the same size and overall shape by differences in their constituent particles.

OCIS codes: (280.1100) Aerosol detection; (290.5855) Scattering, polarization.
http://dx.doi.org/10.1364/OL.39.004076

Real-time detection and characterization of bio-aerosol particles is a crucial technology required to mitigate the threat of biological warfare agents. The strong elastic light scattering resulting from the large optical cross section of bio-aerosol particles provides a natural means for high-speed, noninvasive aerosol characterization [1–6]. For example, the two-dimensional angular optical scattering patterns have been proposed as fingerprints to discriminate between different classes of particles [3–8]. However, interpreting these complex patterns is challenging and has limited the adoption of this technique. Recent theoretical work suggested that the polarization aspect ratio could provide a more robust metric, enabling the differentiation between aggregates composed of particles with different shapes or packing densities [9–11]. Experimental confirmation is required to assess the potential of this technique.

In this Letter, we present an experimental setup capable of measuring the polarization-resolved angular optical backscattering intensity distribution (155°–180°) of airborne aerosol particles in a single laser shot. We used this system to study a series of aggregates composed of different primary particles, including spherical polystyrene particles, elongated *Bacillus subtilis* (BG) particles (a common anthrax simulant) [10], and Arizona road dust (ARD), composed of a mixture of dust particles with varying shape. We observed clearly differentiable polarization aspect ratios in the near-backward direction from the different aggregate types. By leveraging the strong elastic light-scattering properties of airborne particles, this approach could enable high-throughput, noninvasive particle screening, as well as apply to aerosol detection and characterization by light detection and ranging (LIDAR).

The experimental apparatus developed in this work enabled single-shot measurements of the angle-resolved elastic scattering intensity distribution for two perpendicular polarization components from individual aggregates flowing through the detection volume in an aerosol jet stream. A schematic of the experimental apparatus is provided in Fig. 1. The particles passed through the experimental apparatus along the y direction at a position indicated by the "aerosol particle" in Fig. 1(a). A frequency-doubled Nd:YAG laser, producing 70 ns pulses at $\lambda = 532$ nm (Y-70, Spectra-Physics), was used as the probe laser. A linear polarizer and quarter-wave plate were used to provide circularly polarized illumination at the focal position of the aspheric lens ($f = 20$ mm, NA $= 0.54$). Individual particles passed through the focal point and scattered light. Near-backscattered light from the particle was then collimated by the aspheric lens, and a nonpolarizing 50/50 beamsplitter was used to separate the scattered light from the optical path of the Nd:YAG laser, as shown in Fig. 1(a). Two polarizing beam splitters in combination with two

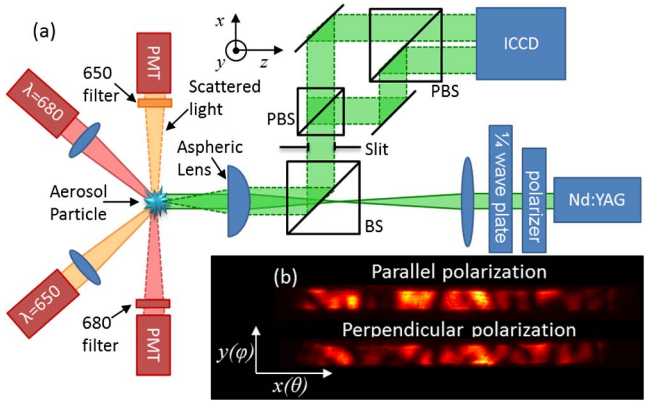

Fig. 1. (a) Schematic of the experimental apparatus. When a particle passes through the focal position where the 650 and 680 nm diode lasers cross, scattered light reaches the PMTs, which trigger the Nd:YAG laser that illuminates the particle and the ICCD camera that records the scattering pattern. Two polarizing beam splitters (PBSs) spatially separated the two polarization components on the ICCD. (b) Typical image recorded on the ICCD showing the backscattering pattern for the two polarizations from an aggregate composed of PSL spheres. The x axis corresponds to scattering in the polar (θ) direction and the y axis to scattering in the azimuthal (φ) direction.

mirrors were then used to spatially separate the perpendicular and parallel polarization components and direct both of these onto the camera, an intensified charge-coupled device (ICCD, Andor iStar). The parallel (perpendicular) polarization component corresponds to scattered light in which the electric field is parallel (perpendicular) to the scattering angle, i.e., the electric field is in the x (y) direction in Fig. 1. In this way, the angle-resolved backscattering intensity distributions for both polarizations were extracted simultaneously from a single image recorded on the camera. A ~2 mm wide slit, oriented perpendicular to the y axis in Fig. 1(a), was placed before the polarizing beam splitters to select a cross section of the scattering pattern to ensure that a line of the patterns from both polarizations could be imaged onto the camera without overlapping. The slit also rejected stray light and multiple reflections from the beam splitter. A typical image recorded on the camera is shown in Fig. 1(b). It presents the angular distribution of the scattering intensity for both polarizations from an aggregate composed of polystyrene latex (PSL) spheres. Different pixels on the pattern correspond to different scattering angles, ranging from nearly 180° (directly back scattered) to 155° in θ horizontally (along the x axis) and a few degrees in φ vertically (along the y axis), where θ and φ are the polar and azimuthal angles in spherical coordinates, respectively. Note that since a rectangular slit was used to select a section of the circular scattering pattern, the angular extent in φ covered ~5° at $\theta = 155°$ and increased as θ approached 180°, potentially limiting the accuracy of our measurement for values of θ close to 180°.

In order to ensure that we only recorded patterns from particles at the focal point of the aspheric lens, two CW diode lasers (operating at $\lambda = 650$ nm and $\lambda = 685$ nm) were used to define the particle position [12]. The two laser beams were oriented approximately perpendicular to each other and focused via a lens to a 100 μm × 100 μm × 100 μm volume ~2 mm above the focal point of the aspheric lens. When a particle crossed the path of one of these CW laser beams, scattered light reached the photomultiplier tubes (PMTs). Interference filters ensured that each PMT was only sensitive to light scattered from one of the CW laser beams. If both PMTs recorded scattering simultaneously (i.e., from the same particle), a triggering signal was sent to the probe laser and the camera to record the scattering pattern of the particle.

In order to calibrate the pixel-to-scattering angle mapping, we first measured the scattering pattern from individual polystyrene spheres, whose scattering pattern can be readily calculated from Mie theory. A Ryco aerosol generator was used to produce a stream of individual PSL particles from a solution of National Institute of Standards and Technology (NIST) traceable 3 μm diameter PSL spheres in water. We recorded the polarization-resolved angular distribution of scattering intensity, similar to the one shown in Fig. 1(b), from 25 PSL spheres. The intensity distribution of each particle was averaged over 20 pixels in the vertical direction, corresponding to averaging over ~2.5° in the φ direction at $\theta = 155°$. In Figs. 2(a) and 2(b), we show the scattering patterns for the parallel and perpendicular polarizations for 25 spheres. We found that each sphere produced a nearly identical scattering pattern, confirming that the

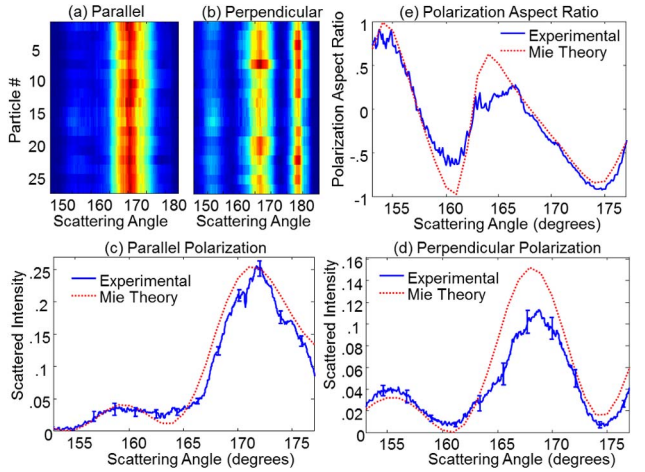

Fig. 2. Scattering intensity distribution for (a) parallel and (b) perpendicular polarizations from 3 μm diameter polystyrene spheres. Each row shows the scattering pattern extracted from an individual sphere. The average scattering pattern over 25 particles is plotted in (c) and (d) for the two polarization components along with the calculation by Mie theory. The error bars indicate the standard deviation over the 25 particles. (e) Polarization aspect ratio of the 3 μm PSL spheres.

system was consistently probing spheres from the same position in front of the aspheric lens, as defined by the two diode laser beams. Based on the size of the probe volume defined by the two crossing laser beams, the angular uncertainty in each measurement was ~0.1°. We then used Mie theory to calculate the scattering pattern from a 3 μm diameter sphere with refractive index of 1.59 at $\lambda = 532$ nm. We then fit the experimental scattering pattern to the simulation by mapping each pixel x to a scattering angle θ. We first identified the pixel that corresponded to backscattering at 180°, which we labeled as x_{180}. We then introduced a second fitting parameter, κ, which was nominally equal to the pixel size divided by the focal length of the aspheric lens. Deviations in κ from its nominal value accounted for the small divergence of the backscattered signal due to imperfect collimation. The scattering angle was then calculated using the Abbe sine condition as $\varphi(x) = 180 - \text{asin}[\kappa(x - x_{180})]$ [13]. After fitting these two parameters, we found the experimentally measured intensity distributions matched the peak and dip positions predicted by Mie theory [Figs. 2(c) and 2(d)]. These scattering patterns were then used to compute the polarization aspect ratio, defined as $P = (I_\perp - I_\parallel)/(I_\perp + I_\parallel)$, shown in Fig. 2(e).

After calibration, we used the experimental apparatus to record the polarization-resolved scattering pattern from a series of aggregate particles. An ink-jet aerosol generator was used to produce aggregates of different primary particles [14]. In practice, the measured polarization and angle-resolved elastic scattering intensity distributions of individual aggregates depend not only on the constituent particles but also on the positions and number of particles within the aggregate, as well as its overall orientation. As a result, the scattering pattern measured from each aggregate is different, even if the aggregates are the same size and composed of the same particles. Figures 3(a) and 3(b) show the angular distribution of scattering intensity for both polarizations

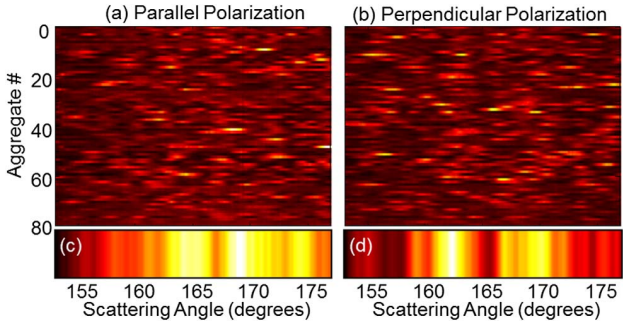

Fig. 3. Scattering intensity distribution for (a) parallel and (b) perpendicular polarizations from 5 to 6 μm polystyrene aggregates composed of 500 nm diameter spheres. Each aggregate exhibits a different scattering pattern depending on its packing density, orientation, and the positions of the individual spheres in the aggregate. Ensemble averaged scattering intensity distribution for the (c) parallel and (d) perpendicular polarizations from the same PSL aggregates.

recorded from a series of ~5.5 μm aggregates composed of 500 nm diameter PSL spheres. Unlike the individual spheres studied in Fig. 2, the scattering pattern of every aggregate is clearly different. As a result, we recorded scattering patterns from at least 200 nominally identical aggregates of each type and then calculated the ensemble-averaged scattering pattern for each polarization.

We considered four types of aggregates: ARD, BG, and PSL aggregates composed of either 500 nm or 1 μm PSL spheres, as well as tryptophan particles. Some typical scanning electron microscope (SEM) images of the particles are shown in the left panel of Fig. 4. The tryptophan particles are dried from solution and condensed to form a solid, near-spherical particle. The ARD aggregates are composed of various dust particles with irregular shapes forming a densely packed aggregate. The BG particles are cylinder-like in shape, with length of ~1 μm and diameter of ~0.5 μm. Finally, the PSL aggregates are composed of spherical particles of 500 nm or 1 μm diameter. A TSI aerodynamic particle sizer (APS 3321) was used to measure the average size of each particle/aggregate. The tryptophan, ARD, BG, 500 nm PSL, and 1 μm PSL particles/aggregates had average sizes of 7.5, 2.3, 5.0, 5.4, and 3.9 μm, respectively.

We recorded the polarization resolved backscattering intensity distributions of 200 particles/aggregates of each type. The polarization aspect ratios of the five particle/aggregate types are shown in the right panel of Fig. 4. The unprocessed experimental data are shown as dotted lines while the solid lines were fit by averaging the experimental data along the polar angle (θ) direction to provide a clearer comparison. This fitting primarily removed the oscillations that were due to averaging over a finite number of particles. The error bars indicate the 95% confidence interval after averaging over 200 particles/aggregates. The particles are arranged from top to bottom in Fig. 4 in approximate order of packing density, with tryptophan being the most densely packed particle and the aggregates composed of 1 μm diameter PSL spheres being the least dense. The polarization ratio of tryptophan exhibits the most pronounced negative polarization of the particles/aggregates considered, exhibiting a minimum value of −0.27. The polarization ratio of ARD and

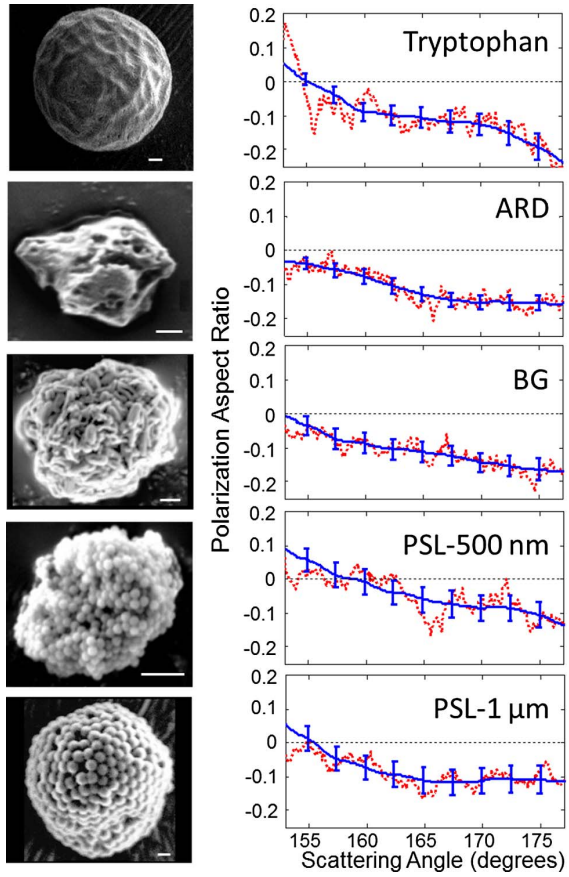

Fig. 4. (Left) Typical SEM images of the 5 particles/aggregates showing their distinct morphologies. The particles/aggregates are ordered according to their approximate packing density from top to bottom. The scale bar in each image represents 1 μm. (Right) Polarization aspect ratios for the 5 particles/aggregates, each averaged over 200 measurements. The red dotted lines represent the unprocessed experimental data, and the solid line is a smoothed fit obtained by averaging the experimental data along the polar angle (θ). The error bars indicate the 95% confidence interval after averaging over 200 aggregates. The negative polarization dip is more pronounced in the more densely packed particles/aggregates.

BG showed intermediate negative polarizations ratios of −0.16 and −0.17, respectively. On the other hand, the negative polarization effect was less pronounced in the less densely packed PSL aggregates, which showed minima of −0.11 and −0.12 for the aggregates composed of 500 nm and 1 μm diameter PSL spheres, respectively. Even considering the measurement uncertainty, the polarization aspect ratios of the different particle/aggregate types are clearly differentiable, confirming that this metric could be used to discriminate between aggregates composed of particles with different shapes. Moreover, this work presents, to our knowledge, the first experimental confirmation that denser particles exhibit more pronounced negative polarization, as predicted by theoretical calculations in the literature [9]. In addition, aggregates composed of more elongated (less spherical) primary particles are predicted to exhibit a more pronounced negative polarization dip [9]. This could also contribute to the more pronounced negative polarization observed in the ARD and BG aggregates as compared with the PSL-based aggregates.

Although we were able to observe the general trend predicted by theory, a few experimental challenges limited our ability to quantitatively match the theoretical predictions. First, the experimental measurements were recorded by averaging over ~200 independent aggregates of each type. Although these aggregates were nominally identical, the inevitable variations in the size, shape, and packing manner of each aggregate introduced additional uncertainty to the measurements. Additionally, unlike in the theoretical calculations, the size and shape of the primary particles in the real aggregates are not identical, and some of these primary particles may be broken during the aggregate formation stage. Residual debris such as surfactants and dust from the water remaining between the primary particles may also affect the measurements. Finally, in our measurement scheme, a rectangular slit was used to select a cross section of the circular scattering pattern, reducing our azimuthal resolution as θ approaches 180°. Despite these experimental challenges, the general trend of density dependent negative polarization was clearly observed.

From a fundamental particle-scattering perspective, one potential limitation of the current approach is the need to average the backscattering patterns recorded from ~200 aggregates or more. This implicitly requires that all of the aggregates in the jet stream are composed of the same primary particles. However, this requirement could be alleviated in a future implementation by leveraging recent advances in the optical trapping of bio-aerosol particles [15]. In such an implementation, the scattering patterns of a single trapped aggregate could be measured from many orientations, providing the required averaging without the need to assume that each aggregate in the jet stream was statistically identical. In addition, such an approach would enable a more accurate match to theoretical predictions, since the polarization ratio could be measured for a single aggregate without averaging over a distribution of aggregates with varying size and shape. However, from a bio-aerosol detection and characterization perspective, the data from this study are more relevant for a LIDAR system, since LIDAR systems generally obtain backscattering information from a group/plume of aerosol particles with different size and shape, similar to the situation presented here.

In summary, we measured the parallel and perpendicular polarization components of the angle-resolved elastic backscattering intensity distributions of individual aerosol particles and aggregates on the fly. We calibrated the system using PSL spheres and found a good match to the scattering intensity distribution predicted by Mie theory. We then used the system to measure the polarization-resolved angular distribution of scattering intensity of aggregates composed of primary particles with different shape and packing density. We observed a significant difference in the polarization aspect ratio between aggregates composed of different primary particles. We also found that the negative polarization was more pronounced in the more densely packed particles/aggregates—the first experimental confirmation, to our knowledge, of the theoretical predictions presented in Ref. [9]. In practice, the polarization aspect ratio could be used in conjunction with additional optical characterization techniques, such as fluorescence [16] and Raman spectroscopy [15], to provide a robust bio-aerosol detection and characterization system. LIDAR-based aerosol classification systems could also benefit from monitoring the polarization aspect ratio at different angles in the near-backward direction rather than only monitoring the ratio at 180° (e.g., [17]).

We thank Gorden Videen and Richard Chang for useful discussions. This work was supported by the Army Research Office under Grant No. W911NF-12-1-0507.

References

1. M. I. Mishchenko, L. D. Travis, and A. A. Lacis, *Scattering, Absorption, and Emission of Light by Small Particles* (Cambridge University, 2002).
2. R. K. Chang, G. E. Fernandes, Y.-L. Pan, K. Aptowicz, and R. G. Pinnick, in *Progress in Electromagnetics Research Symposium* (2007), pp. 622–625.
3. P. J. Wyatt, Nature **221**, 1257 (1969).
4. M. Bartholdi, G. C. Salzman, R. D. Hiebert, and M. Kerker, Appl. Opt. **19**, 1573 (1980).
5. P. H. Kaye, K. Alexander-Buckley, E. Hirst, and S. Saunders, J. Geophys. Res. **101**, 19215 (1996).
6. M. D. Barnes, N. Lermer, W. B. Whitten, and J. M. Ramsey, Rev. Sci. Instrum. **68**, 2287 (1997).
7. P. H. Kaye, Meas. Sci. Technol. **9**, 141 (1998).
8. O. V. Kalashnikova, R. Kahn, I. N. Sokolik, and L. Wen-Hao, J. Geophys. Res. **110**, D18S14 (2005).
9. E. Zubko, Y. Shkuratov, M. Hart, J. Eversole, and G. Videen, Opt. Lett. **28**, 1504 (2003).
10. P. Raman, K. A. Fuller, and D. A. Gregory, Opt. Eng. **52**, 074106 (2013).
11. J. Tyynelä, E. Zubko, K. Muinonen, and G. Videen, Appl. Opt. **49**, 5284 (2010).
12. Y.-L. Pan, M. J. Berg, S. S.-M. Zhang, H. Noh, H. Cao, R. K. Chang, and G. Videen, Cytom. A **79**, 284 (2011).
13. S. Holler, J. Auger, B. Stout, Y.-L. Pan, J. R. Bottiger, R. K. Chang, and G. Videen, Appl. Opt. **39**, 6873 (2000).
14. J. R. Bottiger, P. J. Deluca, E. W. Stuebing, and D. R. Vanreenen, J. Aerosol Sci. **29**, S965 (1998).
15. Y.-L. Pan, S. C. Hill, and M. Coleman, Opt. Express **20**, 5325 (2012).
16. Y.-L. Pan, H. Huang, and R. K. Chang, J. Quant. Spectrosc. Radiat. Transfer **113**, 2213 (2012).
17. X. Cao, G. Roy, and R. Bernier, Opt. Eng. **49**, 116201 (2010).